

**Seismo-Electromagnetic Thin-Bed Responses
Natural Signal Enhancements?**

Grobbe, Niels; Slob, Evert

DOI

[10.1002/2015JB012381](https://doi.org/10.1002/2015JB012381)

Publication date

2016

Document Version

Final published version

Published in

Journal of Geophysical Research

Citation (APA)

Grobbe, N., & Slob, E. (2016). Seismo-Electromagnetic Thin-Bed Responses: Natural Signal Enhancements? *Journal of Geophysical Research*, 121(4), 2460-2479.
<https://doi.org/10.1002/2015JB012381>

Important note

To cite this publication, please use the final published version (if applicable).
Please check the document version above.

Copyright

Other than for strictly personal use, it is not permitted to download, forward or distribute the text or part of it, without the consent of the author(s) and/or copyright holder(s), unless the work is under an open content license such as Creative Commons.

Takedown policy

Please contact us and provide details if you believe this document breaches copyrights.
We will remove access to the work immediately and investigate your claim.



RESEARCH ARTICLE

10.1002/2015JB012381

Seismo-electromagnetic thin-bed responses:
Natural signal enhancements?

Key Points:

- Interference patterns of thin-bed effects on seismo-electromagnetic signals are studied
- Coupling coefficient contrast determines whether interference is constructive or destructive
- Seismo-electromagnetic signals show high sensitivity to oil/water contacts

Correspondence to:

N. Grobbe,
ngrobbe@gmail.com

Citation:

Grobbe, N., and E. C. Slob (2016), Seismo-electromagnetic thin-bed responses: Natural signal enhancements?, *J. Geophys. Res. Solid Earth*, 121, 2460–2479, doi:10.1002/2015JB012381.

Received 21 JUL 2015

Accepted 10 MAR 2016

Accepted article online 14 MAR 2016

Published online 9 APR 2016

N. Grobbe¹ and E. C. Slob¹¹ Department of Geoscience and Engineering, Delft University of Technology, Delft, Netherlands

Abstract We study if nature can help us overcome the very low signal-to-noise ratio of seismo-electromagnetic converted fields by investigating the effects of thin-bed geological structures on the seismo-electromagnetic signal. To investigate the effects of bed thinning on the seismo-electromagnetic interference patterns, we numerically simulate seismo-electromagnetic wave propagation through horizontally layered media with different amounts and thicknesses of thin beds. We distinguish two limits of bed thickness. Below the upper limit, the package of thin beds starts acting like an “effective” medium. Below the lower limit, further thinning does not affect the seismo-electromagnetic interface response signal strength anymore. We demonstrate seismo-electromagnetic sensitivity to changes in medium parameters on a spatial scale much smaller than the seismic resolution. Increasing amounts of thin beds can cause the interface response signal strength to increase or decrease. Whether constructive or destructive interference occurs seems to be dependent on the seismo-electromagnetic coupling coefficient contrasts. When the combined result of the contrast, between upper half-space and package of thin beds and the internal thin-bed contrast, is positive, constructive interference occurs. Destructive interference occurs when the combined contrast is negative. Maximum amplitude tuning occurs for thicknesses of thin-bed packages similar to the dominant pressure and shear wavelengths. Artifacts due to model periodicity are excluded by comparing periodic media with random models. By simulating moving oil/water contacts during production, where the oil layer is gradually being thinned, seismo-electromagnetic signals are proven very sensitive to oil/water contacts. An oil layer with a thickness of <1% of the dominant shear wavelength is still recognized.

1. Introduction

In the field of global geophysics, seismology is the most important tool for imaging the Earth, which makes use of the mechanical waves that are generated due to natural hazards like earthquakes. Also in the field of applied geophysics, seismic imaging plays the key role in exploration. However, besides seismic waves, other types of physical phenomena are increasingly being exploited for geophysical purposes, both for global-scale and exploration-scale purposes. Examples are electromagnetic methods like Induced Polarization [e.g., Marshall and Madden, 1959; Oldenburg and Li, 1994; Reil and Florsch, 2010], Magnetotelluric methods [e.g., Cagniard, 1953; Vozoff, 1972; Colombo and De Stefano, 2007; Carbajal et al., 2012], Ground-Penetrating Radar [e.g., Sambuelli et al., 1999; Guha et al., 2005; Kruse et al., 2006; Feld and Slob, 2014], and Controlled Source Electromagnetics [e.g., Constable, 2010; Hunziker et al., 2011; Colombo et al., 2013; Hunziker et al., 2014]. Furthermore, even within seismic wave studies, different approaches exist as well. Classically, only acoustic waves were being used. In addition, elastodynamic systems are used to describe the pressure and shear wave propagation. More complex systems are being studied increasingly as well, like viscoelastic and poroelastic wave propagation [e.g., Carcione et al., 2010; Rubino et al., 2015]. There have also been studies focusing on interactions between mechanical wavefields and electromagnetic fields. Currently, we know two types of seismo-electromagnetic effects. In 1936, Thompson [1936] showed that an electric field change can occur associated to elastodynamic waves, since the mechanical disturbances change the local resistivity of the medium. He demonstrated this using a setup that actively generates a constant current between two electrodes and that measures the potential difference. While measuring, an elastodynamic wave propagates in the medium, passing by the electrodes and creating a change in potential difference. Thompson [1936] suggested that these measurements could be used to distinguish the propagation direction of different arrivals (for example, horizontal versus vertical propagation). The second type of seismo-electromagnetic effect was first described by Ivanov [1940], who discussed the coupling between mechanical waves and fully coupled

©2016. The Authors.

This is an open access article under the terms of the Creative Commons Attribution-NonCommercial-NoDerivs License, which permits use and distribution in any medium, provided the original work is properly cited, the use is non-commercial and no modifications or adaptations are made.

electromagnetic fields, where the electric and magnetic fields are influencing each other. This is the type of seismo-electromagnetic phenomenon that we investigate in this paper. A theory for wave propagation of electrokinetic phenomena in fluid-saturated porous media was developed by *Frenkel* [1944], in which he predicted the slow compressional wave and the seismo-electromagnetic effect. He made a marginal error in the development of the Biot-Gassmann constants and also only considered the electric effect and not the full Maxwell equations [*Pride and Garambois*, 2005]. It was *Pride* [1994] who derived a set of governing equations describing the seismo-electromagnetic system by coupling Biot's poroelasticity equations to the full Maxwell electromagnetic equations. This boosted the geophysical research on seismo-electromagnetic phenomena. Several laboratory experiments [e.g., *Jouniaux and Pozzi*, 1995; *Zhu and Toksöz*, 2005; *Schakel et al.*, 2011], numerical modeling experiments [e.g., *Haartsen and Pride*, 1997; *Haines and Pride*, 2006; *Garambois and Dietrich*, 2002; *Zyserman et al.*, 2010; *Grobbe and Slob*, 2013; *Kröger et al.*, 2014; *Grobbe et al.*, 2014; N. Grobbe et al., Comparison of eigenvectors for coupled seismo-electromagnetic layered-Earth modeling, submitted to *Geophysical Journal International*, 2015], and field tests [e.g., *Butler et al.*, 1996; *Thompson et al.*, 2007; *Dean et al.*, 2012] have been carried out in attempts to understand this complex physical phenomenon better and to develop applications for the geophysical community.

The seismo-electromagnetic effect takes advantage of subsurface coupling between mechanical wavefields and electromagnetic fields. In this way, seismo-electromagnetic phenomena offer simultaneously seismic resolution and electromagnetic fluid sensitivity. Furthermore, several studies have already shown that the seismo-electromagnetic method can provide us with supplemental information on crucial reservoir parameters like porosity and permeability, as well as sensitivity to pore fluid properties [e.g., *Pride*, 1994; *Haines and Pride*, 2006; *Revil et al.*, 2007; *Smeulders et al.*, 2014]. This can potentially be used, for example, to detect or monitor gas/water or oil/water contacts. Recently, the seismo-electromagnetic effect is also studied for global scale applications, e.g., using seismo-electromagnetic phenomena for the detection of microcracks prior to ruptures generating earthquakes [e.g., *Fujinawa et al.*, 2011; *Ren et al.*, 2012; *Fujinawa and Noda*, 2015].

Currently, one of the major challenges of the seismo-electromagnetic method is the very weak signal-to-noise ratio of the seismo-electromagnetic signals. In order to make the seismo-electromagnetic method feasible for industrial and natural hazard applications, we need to find ways to improve the signal-to-noise ratio of especially this second-order effect. There are some examples of successful field tests [e.g., *Butler et al.*, 1996; *Thompson et al.*, 2007]. However, more real data examples of the seismo-electromagnetic method are required to really bring this method to the next level. Several different attempts have been made over the last couple of years. For example, *Dean and Dupuis* [2011], *Dean et al.* [2012], and *Valuri et al.* [2012] used a large commercial hydraulic vibrator to try and boost the signal-to-noise ratio of the seismo-electromagnetic data. Recently, *Sava and Revil* [2012], *Revil et al.* [2013], and *Sava et al.* [2014] have explored to use seismo-electromagnetic focusing techniques to maximize the seismo-electromagnetic conversion. All of these methods seem to improve the signal-to-noise ratio. However, the desired amplification of the signal for guaranteed successful measurements in the field has not yet been achieved.

But what if nature itself can already help us? From seismics, it is well known that a seismic wave traveling through a package of thin beds can experience amplitude-tuning effects that result in anomalously high amplitudes for the seismic signal [e.g., *Widess*, 1973; *Robertson and Nogami*, 1984]. Can similar enhancing signal effects occur for seismo-electromagnetic phenomena? We start with a brief recapitulation of seismic amplitude tuning effects in thin-bed geological settings, including an extension toward the seismo-electromagnetic scenario. We will then numerically investigate what effects thin beds can have on the seismo-electromagnetic signal, thereby focusing especially on the seismo-electromagnetic conversion. To this end, we use our analytically based, numerical modeling code ESSEMOD (Electromagneto-seismic and seismo-electromagnetic Modeling) [*Grobbe and Slob*, 2013; *Grobbe et al.*, 2014, N. Grobbe et al., submitted manuscript, 2015]. We observe that certain thin-bed geological settings can yield constructive interference of the seismo-electromagnetic responses, amplifying the signal strength with a factor of 3. We will highlight the factors that play a role in this possible enhancement of the seismo-electromagnetic signal strength by thin beds. We study the effects of the seismo-electromagnetic coupling coefficient contrasts by varying the electrolyte concentrations of the pore fluid. The seismo-electromagnetic coupling coefficient is a very important seismo-electromagnetic parameter, since this parameter controls the amount of coupling between the mechanical waves and the electromagnetic fields. At low frequencies, this coefficient is fundamentally the same as the coefficient measured in classical streaming potential laboratory experiments [e.g., *Morgan et al.*, 1989; *Jouniaux et al.*, 2000; *Schoemaker et al.*, 2012]. We finalize by focusing on an oil/water contact in a

reservoir, and by simulating production we will see the effects a varying ratio of oil/water thickness has on the seismo-electromagnetic signals.

2. Theory: Brief Introduction to Seismo-electromagnetics and Thin Beds

Seismo-electromagnetic phenomena can be described by Biot's poroelasticity equations [Biot, 1956] coupled to Maxwell's electromagnetic equations. Using the principle of volume averaging, Pride [1994] derived a set of governing equations for seismo-electromagnetic phenomena in fully saturated porous media. Pride and Haartsen [1996] and Haartsen and Pride [1997] showed how to use these governing equations to describe seismo-electromagnetic wave propagation in horizontally layered, radially symmetric, fluid-saturated porous media. Recently, Warden *et al.* [2013] have extended the theory to deal with partially saturated media as well. Revil and coauthors have developed and tested an alternative formulation of the seismo-electromagnetic theory [e.g., Revil *et al.*, 2003; Jardani *et al.*, 2010; Revil *et al.*, 2015]. In the seismo-electromagnetic theory of Pride [1994], full coupling between the electric and magnetic fields is considered, whereas Revil and coauthors make use of the well-known quasi-static approach for electromagnetic fields, which exploits the fact that at low frequency (which seems to be applicable to the seismo-electromagnetic effect where seismic frequencies are considered), the electric and magnetic parts are not coupled. Hence, the rotation-free electric field can be written as minus the gradient of an electrical potential. Since seismo-electromagnetic phenomena are sensitive to a huge amount of parameters, being able to simplify the system, for example, in this way, might be beneficial for both our understanding of the phenomenon as well as for further developing the technique toward imaging and inversion [e.g., Sava and Revil, 2012; Sava *et al.*, 2014]. In seismo-electromagnetic phenomena, the actual coupling occurs in transport equations that are constituents of Biot's and Maxwell's equations. Different assumptions can be made regarding the physical mechanisms that underlie the model. These assumptions have their effect on the actual model parameters. In the theory as presented by Pride [1994], and as adopted in our paper, he assumes that no wave-induced diffusion effects occur, that there are no chemical gradients present (meaning that there are no free charges induced on the surfaces of the grains), that there is no wave scattering at the scale of the grains, that there are no piezoelectric or other anisotropic effects occurring, and that the disturbances that happen in the medium only have linear effects. Furthermore, the pore fluids are assumed to be ideal electrolytes. It is important to realize that these postulates that Pride [1994] states, affecting the dynamic coupling coefficient and permeability as well as the electrical conductivity, are not per definition the correct ones. Revil and Mahardika [2013] present an elegant alternative using other assumptions. This results in theoretical complex conductivity expressions that agree with experimentally observed quadrature conductivities. Their formulation allows for investigating seismo-electromagnetic effects (so in this case no quasi-static approach is used) in unsaturated porous media. Recently, Jardani and Revil [2015] extended the theory for full coupling in two-phase flow media.

Two types of seismo-electromagnetic coupling can be distinguished (see Schoemaker *et al.* [2012], for a schematic illustration): First of all, localized coupling generating an electromagnetic field that is present inside the seismic wave and travels with seismic velocity is referred to as the coseismic field. Since the coseismic field is generated locally it can only provide us with localized information close to the receivers. This effect might therefore be useful for borehole applications, such as those discussed by, e.g., Zhu *et al.* [2000] and Zhu and Toksöz [2005]. Another borehole application might be to map the permeability close around the well with the purpose of determining where to optimally perforate the well casings.

The second type of coupling is referred to as the seismo-electromagnetic conversion or interface response (IR) field. This second-order coupling effect yields an independent electromagnetic field diffusing with electromagnetic velocity, which is generated whenever there is a contrast in mechanical, hydraulic or electrical medium parameters. The electromagnetic diffusive velocity is several orders of magnitude higher than the seismic wave velocities. These diffusive electromagnetic events will arrive almost instantaneously at the receiver level, and hence, these IR events will show up in seismoelectrograms as more or less horizontal events at one-way seismic traveltime (the seismic traveltime from the source to the generating interface). These converted fields can provide us with information at depth and are therefore of primary interest when exploiting seismo-electromagnetic methods in industry. However, since these fields are second-order coupling effects, their signal-to-noise ratio is very low. The IR fields might also be useful in borehole scenarios, if the receivers are then located close to the target area of interest, and hence, less amplitude losses will occur for the diffusive electromagnetic fields.

In addition, seismo-electromagnetic conversion occurs directly at the source, where, for example, an instantaneous electromagnetic field is being generated upon seismic source impact. This is sometimes referred to as a third type of seismo-electromagnetic signal [see, e.g., *Revil et al.*, 2015].

Despite possible borehole applications, the main challenge for the seismo-electromagnetic method remains to be able to boost the signal-to-noise ratio of the events. In the field of seismic exploration, it is well known that when a seismic wave travels through a package of thin layers (with appropriate amplifying thickness), amplitude-tuning effects can occur resulting in anomalously high amplitudes [*Robertson and Nogami*, 1984]. The big question is, can similar naturally signal-enhancing effects occur for seismo-electromagnetic phenomena? Since the seismo-electromagnetic effect is a complex physical phenomenon of which very little is still understood, the exact effect of a seismo-electromagnetic wave propagating through a package of thin beds is unpredictable. However, one can intuitively understand that constructive interference might take place. Let us consider the following thought experiment: since the IR fields arrive almost instantaneously at one-way seismic traveltime, an incremental increase in seismic traveltime (due to, for example, downward wave propagation through a thin bed) followed by a seismo-electromagnetic conversion at the bottom interface of the thin bed (that arrives instantaneously on seismic timescales), might result in constructive interference of the recorded IR fields. In other words, when the one-way seismic traveltime is not increasing too much, the generated IR field of the bottom interface of a certain thin bed might map constructively on the generated IR field of the top interface of the thin bed. The possibility of IR field enhancing effects due to the presence of a thin bed has been discussed in *Pride and Garambois* [2005], where they show that the amplitude of the converted electric field can be drastically increased (by a factor of 10 in their example of a thin shale layer), if there is a thin layer of a third type of material present close to the interface that generates the IR field. Furthermore, *Dietrich and Garambois* [2013] discuss a possible super-resolution of very thin layers using the seismo-electromagnetic conversions. When studying seismo-electromagnetic thin-bed responses, important questions to ask are, of course: What is the subseismic resolution limit for seismo-electromagnetic sensitivity? Does an increase in the amount of thin beds necessarily lead to an increase of the IR field signal strength? What parameters play a role in determining whether constructive or destructive interference occurs? Do different pore fluid contrasts and relative thicknesses have an effect on the interference pattern? As *Widess* [1973] already acknowledges, how thin is a thin bed? Seismically speaking, based on reflective properties, a thin bed may be defined as a bed with a thickness that is less than $\lambda_{\text{peak}}/8$. In this case, the reflections of the top and bottom edges of the thin-bed interfere constructively [*Zhou*, 2014]. Here λ_{peak} is the dominant wavelength for the seismic velocity of the bed [*Widess*, 1973], determined by the relation between peak frequency of the source wavelet and the seismic wave velocity of the layer under consideration. In addition, *Widess* [1973] observed that for bed thicknesses smaller than the tuning thickness, the composite wavelet approaches the derivative of the basic wavelet [*Zhou*, 2014]. It is important to realize that when geologists speak of thin beds, they often refer to beds of a few centimeters to meters thick, whereas the seismic definition of a thin bed can result in much thicker beds. As an example, consider a peak frequency of a wavelet of 30 Hz and a medium with a *P* wave velocity of 3000 m/s, which results in a peak wavelength of 100 m. According to *Widess* [1973], every bed with a thickness of 12.5 m or less is considered a thin bed. Geologically speaking, according to the seismic definition, most beds in nature are then a thin bed. For seismo-electromagnetics, it is yet unknown what should be considered as a thin bed, if tuning effects or wavelet shape changes occur, and for which bed thicknesses the seismo-electromagnetic signals are not sensitive anymore.

3. Method: Numerical Modeling

To investigate the effects of thin beds on seismo-electromagnetic signals, we make use of our analytically based, numerical modeling code for layered Earth systems ESSEMOD [*Grobbe and Slob*, 2013; *Grobbe et al.*, 2014, N. Grobbe et al., submitted manuscript, 2015]. ESSEMOD is capable of modeling all existing electroseismic and seismo-electromagnetic source-receiver combinations. In this study, we focus on the effect of thin beds on the most common seismo-electromagnetic source-receiver combination, a horizontal electric field component E_1 in the x_1 direction due to a horizontal seismic dipole bulk force source F_1^b (for example, a seismic shear wave vibrator) in the same x_1 direction. Of course, a similar numerical study can be carried out focusing on other source-receiver combinations.

We simulate seismo-electromagnetic wave propagation through layered-Earth configurations with different amounts and thicknesses of thin beds to study the effect of bed thinning on the amplification or weakening

Table 1. Overview of the Velocities of the Different Field Types, Input Medium Parameters, and Relevant Petrophysical Parameters Determining the Static Coupling Coefficient for Each of the Different Media^a

Physical Quantity	Medium A (Top hs)	Medium B (Layer or hs)	Medium C (Layer or hs)
Fast P wave velocity (m/s)	3159.81–3159.84	3153.67–3153.68	3348.94–3349.00
Slow P wave velocity (m/s)	2.89–92.96	3.98–131.09	5.46–189.62
S wave velocity (m/s)	2110.79–2110.87	1952.83–1953.03	1886.09–1886.70
Electromagnetic (EM) velocity (m/s)	31796.34–1005899.70	4496.68–142233.40	20109.77–636104.47
Static coupling coefficient \mathcal{L}_0 (m^2sV^{-1})	$9.07 \cdot 10^{-9}$	$2.08 \cdot 10^{-9}$	$1.65 \cdot 10^{-9}$
Zeta potential double layer ζ^P (V)	$-9.6 \cdot 10^{-2}$	$-4.4 \cdot 10^{-2}$	$-7 \cdot 10^{-2}$
Electric conductivity fluid σ^f (S m^{-1})	$9.27 \cdot 10^{-3}$	0.93	$9.27 \cdot 10^{-2}$
Complex electric conductivity $\hat{\sigma}^e$ (S m^{-1})	$1.24 \cdot 10^{-3}$	$6.18 \cdot 10^{-2}$	$3.09 \cdot 10^{-3}$
Porosity ϕ (-)	0.4	0.2	0.1
Electric permittivity vacuum ϵ_0 (F m^{-1})	$8.85 \cdot 10^{-12}$	$8.85 \cdot 10^{-12}$	$8.85 \cdot 10^{-12}$
Relative electric permittivity fluid ϵ_r^f (-)	80	80	80
Relative electric permittivity solid ϵ_r^s (-)	4	4	4
Fluid density ρ^f (kg m^{-3})	$1 \cdot 10^3$	$1 \cdot 10^3$	$1 \cdot 10^3$
Solid density ρ^s (kg m^{-3})	$2.7 \cdot 10^3$	$2.7 \cdot 10^3$	$2.7 \cdot 10^3$
Shear modulus framework grains G^{fr} (N m^{-2})	$9 \cdot 10^9$	$9 \cdot 10^9$	$9 \cdot 10^9$
Viscosity pore fluid η (N s m^{-2})	$1 \cdot 10^{-3}$	$1 \cdot 10^{-3}$	$1 \cdot 10^{-3}$
Static permeability k_0 (m^2)	$1.3 \cdot 10^{-12}$	$1.6 \cdot 10^{-12}$	$2.2 \cdot 10^{-12}$
Tortuosity α_∞ (-)	3.0	3.0	3.0
Bulk modulus framework grains K^{fr} (N m^{-2})	$4 \cdot 10^9$	$4 \cdot 10^9$	$4 \cdot 10^9$
Bulk modulus solid K^s (N m^{-2})	$4 \cdot 10^{10}$	$4 \cdot 10^{10}$	$4 \cdot 10^{10}$
Bulk modulus fluid K^f (N m^{-2})	$2.2 \cdot 10^9$	$2.2 \cdot 10^9$	$2.2 \cdot 10^9$
Electrolyte concentration pore fluid C (mol L^{-1})	$1 \cdot 10^{-4}$	$1 \cdot 10^{-2}$	$1 \cdot 10^{-3}$
pH (-)	7	7	7
Ionic mobility of cations b^+ ($\text{m s}^{-1} \text{N}^{-1}$)	$3 \cdot 10^{11}$	$3 \cdot 10^{11}$	$3 \cdot 10^{11}$
Ionic mobility of anions b^- ($\text{m s}^{-1} \text{N}^{-1}$)	$3 \cdot 10^{11}$	$3 \cdot 10^{11}$	$3 \cdot 10^{11}$
Similarity parameter m (-)	8	8	8

^aTo illustrate the frequency dependency of certain wave/field types, velocity ranges (the real parts of the complex velocities) are displayed for the bandwidth under consideration. Note that the EM-velocities are proportional to the square root of frequency.

of the IR fields. To fully focus on the effect of the thin beds we use two very simple reference configurations consisting of two homogeneous half-spaces (hs), either medium A and medium B or medium A and medium C.

In Table 1, we present the effective seismo-electromagnetic velocities of the different field types, the input medium parameters, and the relevant petrophysical parameters determining the static coupling coefficient, for each of the different media. We can observe that the dominant factor is the change in porosity of the medium. The shear waves are more affected by a porosity change than pressure waves (the pores are saturated with fluid, so higher porosity means more fluid), which explains why the P wave velocity does not vary as much as the shear wave velocity does.

The seismo-electromagnetic coupling coefficient is the coefficient that controls the amount of coupling between elastic waves and electromagnetic fields in porous media and therefore plays a crucial role in seismo-electromagnetic studies. As discussed in section 1, different underlying theoretical assumptions can lead to different expressions for the dynamic coupling coefficient, the dynamic permeability, and the complex conductivity. Since we follow the assumptions as made by *Pride* [1994], the expressions for these three important parameters are

$$\hat{\mathcal{L}} = \mathcal{L}_0 \left[1 + \frac{s}{\omega_c} \frac{m}{4} \left(1 - 2 \frac{d^l}{\Lambda} \right)^2 \left(1 - d^l \sqrt{\frac{s \rho^f}{\eta}} \right)^2 \right]^{-\frac{1}{2}}, \quad (1)$$

$$\hat{k} = k_0 \left[\left(1 + \frac{s}{\omega_c} \frac{4}{m} \right)^{\frac{1}{2}} + \frac{s}{\omega_c} \right]^{-1}, \quad (2)$$

$$\hat{\sigma}^e = \frac{\phi\sigma^f}{\alpha_\infty} \left[1 + \frac{2(C_{em} + \hat{C}_{os})}{\sigma^f \Lambda} \right], \quad (3)$$

where we used an opposite definition of the Fourier transform compared to *Pride* [1994]. The “hat” symbol indicates frequency dependency (in the space-radial frequency domain). For notational convenience, we introduced in our notation the Laplace parameter $s = j\omega$. In equation (1), m is the similarity parameter, representing a combination of pore geometry parameters. The similarity parameter is a dimensionless number that will be fixed to a value of 8 [Johnson *et al.*, 1987; Johnson, 1989]. Furthermore, Λ represents the volume-to-surface ratio of the porous material and d^l the Debye screening length [e.g., *Pride*, 1994; *Schoemaker et al.*, 2012]. The fluid density is indicated with ρ^f , and η represents the viscosity of the pore fluid. In addition, \mathcal{L}_0 represents the static coupling coefficient, which is defined as [Garambois and Dietrich, 2001; *Pride and Garambois*, 2005]

$$\mathcal{L}_0 = -\frac{\phi\epsilon_0\epsilon_r^f\zeta^p}{\alpha_\infty\eta} \left(1 - 2\frac{d^l}{\Lambda} \right), \quad (4)$$

where ϕ is the porosity (as a volume fraction), ϵ_0 and ϵ_r^f are the electric permittivity of vacuum and the relative electric permittivity of the fluid, respectively, and α_∞ represents the tortuosity of the porous medium, a parameter describing the pore geometry. An important parameter is ζ^p , the zeta potential. This is an electrical potential that quantifies the mobile excess charge in the electrochemical double layer [e.g., *Morgan et al.*, 1989; *Schakel and Smeulders*, 2010]. When the zeta potential is equal to zero, no electrokinetic coupling is induced. In equation (2), k_0 represents the static permeability. Looking at equation (3), we can recognize an excess conductance term C_{em} that is associated with electromigration of excess charge and a dynamic excess conductance term \hat{C}_{os} that is related to electroosmosis. Important in both equations (1) and (2) is ω_c , representing the critical frequency separating the low-frequency viscous flow regime from the high-frequency inertial flow regime, defined as

$$\omega_c = \frac{\phi\eta}{\alpha_\infty k_0 \rho^f}. \quad (5)$$

For realistic rock and fluid parameters and general field scenarios, this transition frequency lies above the maximum frequency of interest (this maximum being roughly between 10 and 1000 Hz). Therefore, the dynamic coupling coefficient can be reduced to the static coupling coefficient, which, in the limit where $\frac{d^l}{\Lambda}$ is small, can be written as [Garambois and Dietrich, 2001; *Pride and Garambois*, 2005]

$$\mathcal{L}_0 = -\frac{\phi\epsilon_0\epsilon_r^f\zeta^p}{\alpha_\infty\eta}. \quad (6)$$

A similar reasoning holds for the dynamic permeability, which can be approximated by the static permeability for the frequency range of interest. The frequency-dependent electroosmotic conductance term in (3) does not cause relaxation in the electrical conductivity for the frequency band under consideration. Therefore, following *Pride and Garambois* [2005], we can use the following reduced static expression (to leading order in $\frac{d^l}{\Lambda}$) for the conductivity

$$\hat{\sigma}^e = \frac{\phi\sigma^f}{\alpha_\infty}. \quad (7)$$

We use $Nt = 2048$ time samples with a time-sampling step of $\Delta t = 0.001$ s. The amount of radial frequencies is $N\omega = Nt/2 + 1$ and the radial frequency sampling step $\Delta\omega = 2\pi/(Nt \cdot \Delta t)$ rad s^{-1} . The wavelet is a causal, first derivative of a Gaussian with peak frequency of 30 Hz and an amplification factor of $1 \cdot 10^9$. Let us start with the reference configuration of hs A above hs B. We now define a package of certain package thickness PT , which we insert in between hs A and hs B (see Figure 1). We consider configurations with $PT = 20, 40, 80,$ and 160 m. In addition, we consider $PT = 70$ and 105 m, which correspond to the dominant wavelength of the shear (S) wave and the Biot fast pressure (P) wave, respectively. According to *Widess* [1973], the minimum seismic thin-bed thickness then reads by definition $\lambda_{peak}/8 = 105/8 = 13.125$ m for P waves and $\lambda_{peak}/8 = 70/8 = 8.75$ m for S waves.

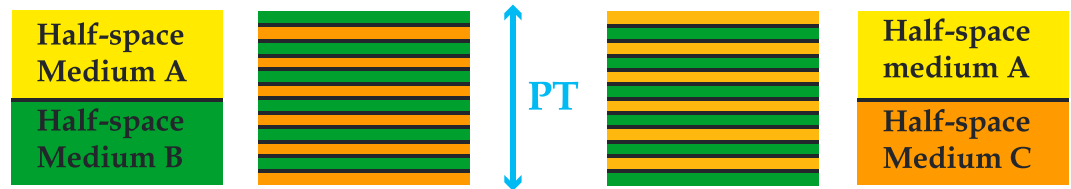


Figure 1. Schematic overview of the two reference configurations and the inserted packages of thin beds, with a total package thickness PT .

We divide the package PT into an even amount of thin beds Nl . The layers alternate between medium B and medium C or vice versa. We consider the following amounts of sublayers: $Nl = 2, 4, 8, 16, 32$, and for $PT > 40$ m also $Nl = 64$. By fixing the package thickness and dividing it consistently into different amounts of thin beds, the bed thickness changes accordingly. In this way both the effects of bed thickness and amount of beds can be investigated.

4. Results

In this section, we present the results of the various numerical thin-bed experiments. We first present the results of the model A-B-C-B, which yields constructive interference. We look at both the effects of varying package thicknesses, varying bed thicknesses, and varying amounts of sublayers. Then, we present the results of model A-C-B-C, which leads to destructive interference. To exclude possible artifacts due to the periodicity of the models used, we compare these results with a model with arbitrary bed thicknesses and a model with random bed thicknesses. Here arbitrary means manually chosen by the user in an arbitrary fashion and random means mathematically random. We slowly increase the amount of sublayers with varying bed thicknesses for a total package thickness PT of 80 m. To study the effect of coupling coefficients on the interference patterns, we focus on varying electrolyte concentrations in the pore fluid. We finalize by investigating the sensitivity of the model to different saturating fluids, namely, an oil/water contact in a porous rock. We simulate oil production where the thickness of the oil layer compared to the water layer thickness starts varying.

4.1. Constructive Interference

Let us start with the configurations A-B-C-B, A-B-C-B-C-B, and so on. We model the reference response as hs A above hs B. A right-handed Cartesian spatial coordinate system is considered, where x_3 is pointing downward representing depth. The source is located at $x_3 = 100$ m and the receivers are placed at $x_3 = 700$ m. The interface that separates the bottom of hs A from the top of the inserted thin-bed package is located at $x_3 = 1000$ m depth (or in other words, this is the interface separating hs A from hs B in the reference response). Considering the seismic wave velocities of medium A (see Table 1), we expect the generated IR fields to arrive at one-way seismic time $t = 0.285$ s for the P wave-associated IR field (from now on referred to as PIR), and at $t = 0.427$ s for the IR field generated by an S wave (referred to as SIR). The rest of the visible events represent coseismic wavefields. Note that for this specific medium configuration and acquisition scenario, the

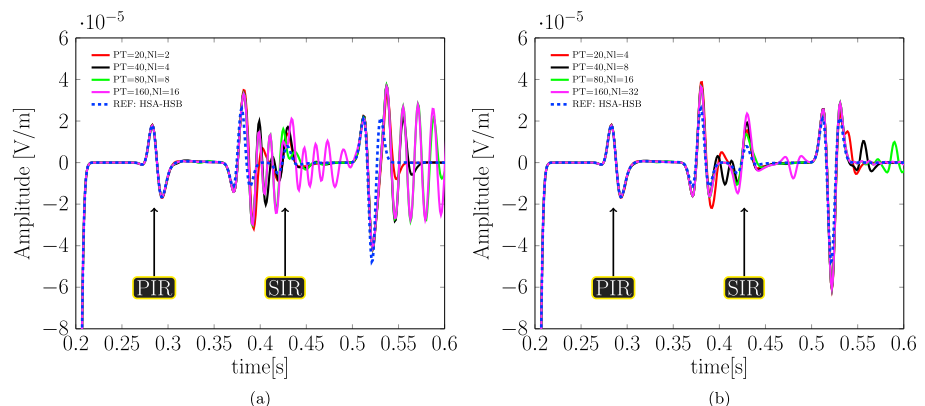


Figure 2. Response for thin-bed geometries of the form A-B-C-B, for different package thicknesses PT with equal individual bed thicknesses of (a) 10 m and (b) 5 m.

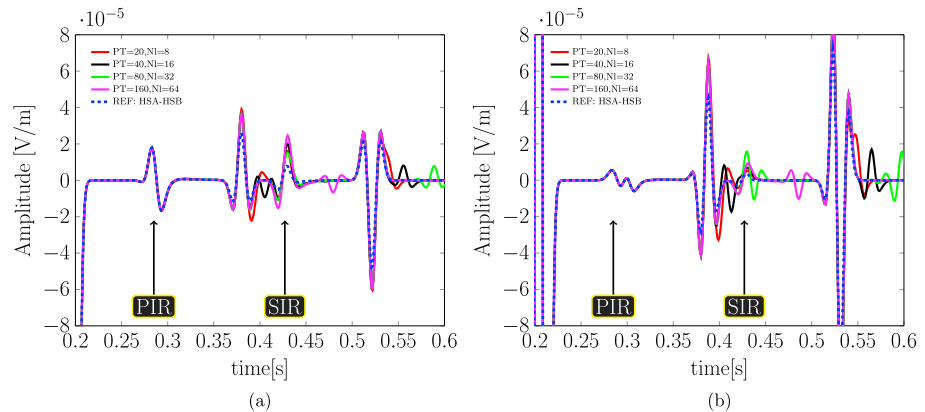


Figure 3. Response for thin-bed geometries of the form A-B-C-B, for different package thicknesses PT with equal individual bed thicknesses of 2.5 m (a) at zero offset and (b) at 140 m offset.

event marked as PIR is actually a combination of the P wave-associated IR field and the coseismic field associated with the direct shear wave from the source to the receiver level. Both events arrive more or less at the same time in the seismo-electromagnetic record, especially at zero offset. We will evaluate this event more carefully later on.

We first present the seismo-electromagnetic thin-bed responses for different package thicknesses PT with equal bed thicknesses (and hence different amounts of thin beds NI per package thickness). Figure 2a presents the results for bed thicknesses of 10 m and Figure 2b for bed thicknesses of 5 m. The reference response is the response when PT = 0 and hence NI = 0. Looking at Figure 2, several observations can be made. We can clearly observe that the PIR signal at $t = 0.285$ s is not strengthened or weakened at all due to the presence of thin beds. The SIR at $t = 0.427$ s, on the other hand, is clearly affected by the thin beds. The differences in sensitivity, between the PIR and SIR responses, to specific contrasts in medium parameters are determined by the reflection coefficients of these conversions. To analyze these effects in greater detail, the reflection behavior of these conversions needs to be studied separately. This is beyond the scope of this paper. Figure 2a shows that for bed thicknesses of 10 m, multiples are visible which are not present in the reference response. In this case, the signal can still distinguish between the individual layers. There seems to be a slight increase of the SIR amplitude with increasing NI, but overall, the beds are still too thick to yield significant constructive or destructive interference. Figure 2b shows that for PT = 20 m and PT = 40 m, multiples are still visible for bed thicknesses of 5 m, whereas for PT = 80 and PT = 160 m, the multiples start vanishing. Furthermore, PT = 160 m displays the largest SIR amplification. Hence, increasing amounts of thin beds of the same thickness (in this case 5 m) can cause the multiples to start vanishing at a certain point (in this case for PT = 80 or larger) and the SIR to increase. Nevertheless, we can also observe that the SIR does not necessarily increase with increasing NI. Figure 3a presents the zero-offset results for bed thicknesses of 2.5 m. Similar patterns can be observed as in Figure 2. Comparing the results for different PT with the reference response, we see that for PT = 20 and PT = 40, additional multiples are still visible before the SIR compared to the reference response, whereas these multiples vanish again with increasing PT and hence increasing NI. Overall, increasing NI seems to yield an increase in SIR strength. Figure 3b shows the same results but now for 140 m offset. We can see that the shape of the PIR event changes with offset, but there is still no visible signal interference due to the presence of thin beds. The SIR reference response is slightly diminished. In addition, the highest signal strength now occurs for PT = 80, instead of PT = 160. Furthermore, PT = 80 now shows an additional multiple just after the SIR response, indicating that for greater offsets, not all multiples are compressed yet for the amount of sublayers in PT = 80. This can be explained in terms of the apparent thicknesses of the beds, which can vary with offset.

Let us study the offset behavior of the thin-bed interference patterns more closely. Figure 4 displays the constructive interference patterns with increasing amounts of thin beds for a package thickness of 40 m, at different offsets. Figure 4a represents the zero-offset trace, Figure 4b shows the interference behavior at different offsets, ranging from -240 m to 240 m.

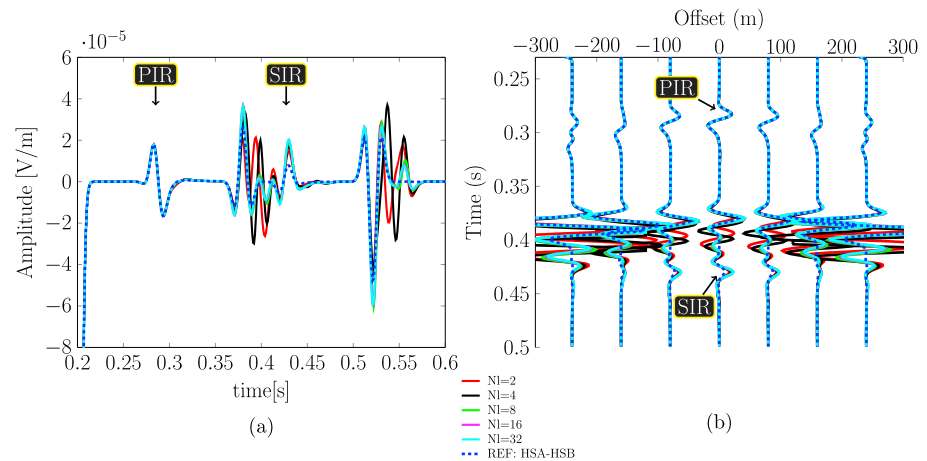


Figure 4. Response for thin-bed geometries of the form A-B-C-B, for a package thickness $PT = 40$ m and increasing amounts of thin beds NI . (a) Zero-offset trace, (b) interference behavior at different offsets, ranging from -240 m to 240 m. Starting at -240 m, we display each eighth trace with 10 m receiver spacing.

We can observe that, as concluded before, constructive interference occurs for the SIR signal, with increasing signal strength for an increasing amount of thin beds. This behavior is visible not only at zero offset (Figure 4a) but also at larger offsets (Figure 4b). However, the SIR signal itself becomes weaker with increasing offset. The PIR response is not visibly affected by the presence of (varying amounts of) thin beds. Not only at zero offset but also for all offsets. The P wave-related seismo-electromagnetic interface response coupling occurs mainly at normal incidence, in the first Fresnel zone [Garambois and Dietrich, 2002]. The offset behavior visible in Figure 4b displays the offset behavior of the electric field that is the result of a seismic-to-electromagnetic interface conversion mainly at normal incidence. In that sense, it does not capture the offset behavior of the incoming seismic wave at the interface. However, as stated earlier, the PIR-indicated event for this specific configuration and medium is actually a combination of the P wave-related interface response field and the direct coseismic shear wave. This can also be observed looking at the larger offsets, where the waveform changes and displays a mixture of two events: one displaying the seismic moveout of the direct coseismic shear wave, the other corresponding to the more or less instantaneously arriving (and hence horizontal) interface response field. The relative contributions of each event to the signal strength are hard to distinguish in this scenario. To purely study the effects of bed thinning on the P wave-related interface response field only, we consider, solely for this specific experiment, a different acquisition geometry for the same model, where

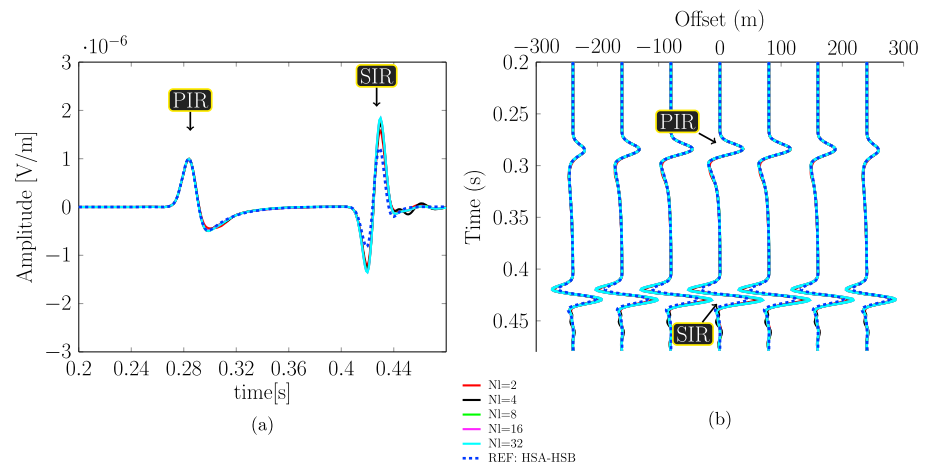


Figure 5. Response for thin-bed geometries of the form A-B-C-B, for a package thickness $PT = 40$ m and increasing amounts of thin beds NI . In this specific example, the source is located at 100 m depth, but the receivers are now located at 300 m depth. The rest of the model is identical to the other models. (a) Zero-offset trace, (b) interference behavior at different offsets, from -240 m to 240 m. Starting at -240 m, we display each eighth trace with 10 m receiver spacing.

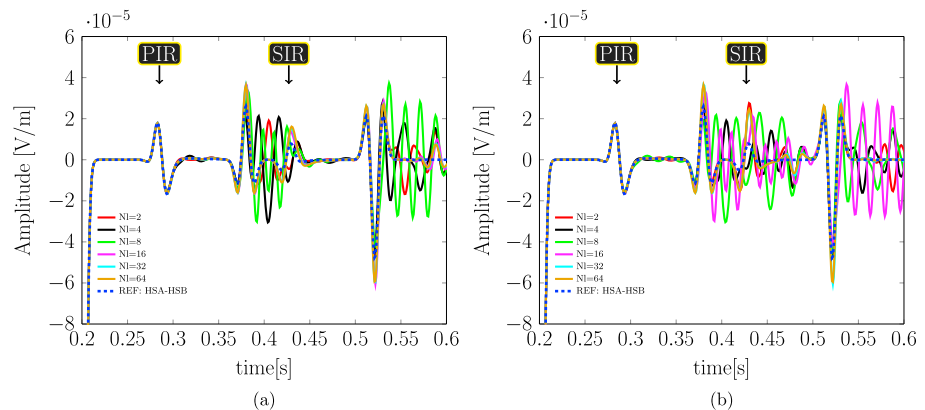


Figure 6. Response for thin-bed geometry A-B-C-B, varying with the amount of layers NI, for a package thickness of (a) 80 m and (b) 160 m.

the source is still located at 100 m depth, but the receivers are now located at 300 m depth. This changes the arrival times of the direct and reflected coseismic fields, but not the one-way seismic arrival times of the interface response fields. Figure 5 presents the results of this study. In Figure 5a, we display the zero-offset trace for a package thickness of 40 m and an increasing amount of thin beds. The record only displays the pure P wave-related interface response field and the S wave-related interface response fields. The direct and reflected coseismic fields (both P and S wave related), are arriving at times outside the chosen time window. We can clearly observe the constructive interference occurring for the SIR event, with increasing amounts of thin beds. We can also observe that the PIR event is visibly not affected by the bed thinning and amounts of thin beds. These observations also hold for other offsets (Figure 5b). In addition, we see that the PIR and SIR events both have smaller absolute amplitudes than in Figure 4a. This is logical due to the longer path that the diffusive interface response EM fields require in the scenario of Figure 5a, before they reach the receiver level. Comparing the PIR events in Figures 4b and 5b, we can clearly observe that the moveout behavior is different in both cases. In Figure 4b, the PIR event clearly displays a seismic moveout behavior as well, whereas in Figure 5b the PIR event is more or less horizontal. This shows that the PIR event in the other experiments are indeed a combination of the P wave-related IR field and the direct coseismic shear wave. Nevertheless, Figure 5b proves that the pure P wave-related IR field is indeed not affected by the amounts of thin beds present and the bed thinning, so our observations regarding this aspect are consistent. Furthermore, we can see that the reference PIR amplitude is smaller than the reference SIR amplitude in Figure 5b, whereas in Figure 4b the reference PIR amplitude is slightly larger than the reference SIR amplitude. This might be an indication of the relative contribution of the direct coseismic shear wave and the P wave-related IR field in Figure 4b. On the other hand, it might also be (partially) related to different diffusive field attenuation rates for the PIR and SIR fields, in relation to the distance between the interface and the receiver level. Since we have demonstrated that the PIR response is not visibly affected by the presence of thin beds, for the model parameters and seismo-electromagnetic source-receiver type combination under consideration, we now continue with our original acquisition geometry, having sources located at 100 m depth and receivers at 700 m depth.

To take a closer look at the effects of increasing NI in a certain PT, we show in Figure 6 the seismo-electromagnetic response for a thin-bed geometry A-B-C-B, varying with the amount of layers NI for a fixed package thickness of either $PT = 80$ m in Figure 6a or $PT = 160$ m in Figure 6b. We can observe that the generated multiple train caused by relatively “thick” beds, at low values for NI and relatively high PT, is compressed with increasing NI and correspondingly decreasing bed thickness. The individual beds are slowly not sensed anymore by the signal and as a result the multiples vanish and the package of thin beds starts acting like an effective medium. In this way the multiples start “mapping” at the arrival time of the SIR. Hence, one can intuitively understand that increasing amounts of thin beds can lead to an increased IR signal strength. This is what we also observed in Figures 2 and 3. One can argue that as soon as all multiples have been compressed, the maximum signal strengthening has been achieved. We can observe that the seismo-electromagnetic signal is still affected for a while by the amount of thin beds even when the individual beds are already not recognized anymore (no multiples). Another way to look at this is that further thinning of the sublayers, at a certain

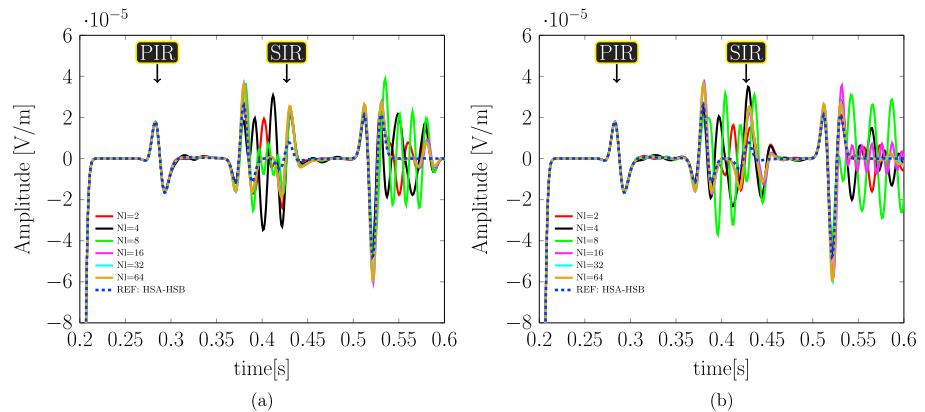


Figure 7. Response for thin-bed geometries of the form A-B-C-B, varying with the amount of layers NI for packages with tuning thicknesses of (a) 70 m (dominant shear wavelength) and (b) 105 m (dominant pressure wavelength).

point, does not improve the signal strength of the IR fields anymore, since the thickness is below the sensitive resolution of the seismo-electromagnetic fields. Illustrative examples can be found comparing the signal of NI = 32 with the signal of NI = 64 for PT = 80 in Figure 6a. So, we can distinguish two limits of bed thickness: an upper limit and a lower limit. The upper limit of bed thickness determines whether the individual layers are still recognized or not. When beds are thinner than this limit, the package of thin beds starts acting like an effective medium and the multiples vanish from the record. The lower limit of bed thickness determines the border from whereon further thinning does not affect the seismo-electromagnetic IR signal strength anymore, because the bed thickness is below the sensitive resolution of the seismo-electromagnetic fields.

From the results of Figures 2, 3, and 6, we can conclude that both the thickness of the thin beds as well as the amount of thin beds play a role in whether or not the multiples (created by the individual thin beds) vanish in the record (i.e., are compressed at the SIR of the reference response). The upper limit seems to occur when the thin-bed thickness reaches a value of around 5 m thickness (and NI > 16). This corresponds to thicknesses of 1/14 and 1/21 of the dominant *S* and *P* wavelengths, 70 m and 105 m, respectively. The lower limit, from whereon further thinning does not affect the signal strength anymore, seems to occur around 2.5 m thickness. This lower limit corresponds to 1/28 and 1/42 of the dominant *S* and *P* wavelengths, respectively. An important anomaly to the general pattern described above can be observed in PT = 160, for NI = 2. In this case the individual bed thicknesses equal 80 m, which is around the dominant *S* wavelength. This observation stimulates *P* and *S* wave tuning experiments, where the amount of thin beds is increased each with a bed thickness of either the dominant *P* or *S* wavelength. These experiments showed that for both cases, increasing NI did not make a difference for the amplifying effect and the results are not displayed here. In another tuning experiment, we focus on the package thickness PT. The results are displayed in Figure 7. We look at the interference patterns for varying NI in tuning package thicknesses of PT = 70 m (Figure 7a) or PT = 105 m (Figure 7b). We can observe that in both cases, there seems to be a maximum strengthening of the *S* wave-related IR signal of a factor 3, higher than we have observed in the earlier presented experiments. This is an indication that not only the amount of thin beds NI and the thin-bed thickness but also the package thickness PT itself plays an important role in the amplification of the SIR due to thin-bed geological structures.

4.2. Destructive Interference

Let us now look what happens if we change the order of the thin beds, i.e., looking at configurations like A-C-B-C with reference response *h_s*-A-*h_s*-C. Except the change in the order of the thin beds, the modeling experiment is identical to the experiment discussed above. In Figure 8, displaying the results of these experiments, similar observations can be made as before in Figures 2–7, except that now increasing NI leads to a decreased signal strength of the *S* wave-related IR field. Looking at the medium properties of media B and C, two main differences can be observed. First, the contrast in electromagnetic velocity between medium B and medium A is much larger than between medium C and medium A. Second, the coupling coefficient of medium B is larger than the one of medium C and therefore forms a smaller difference with the highest coupling coefficient, that of medium A. Hence, the contrast in coupling coefficients between medium A and package of thin-beds PT is positive (i.e., the upper layer has a higher value than the lower layer of the contrast under consideration). Intuitively, one can imagine that the contrast in coupling coefficients plays an important role

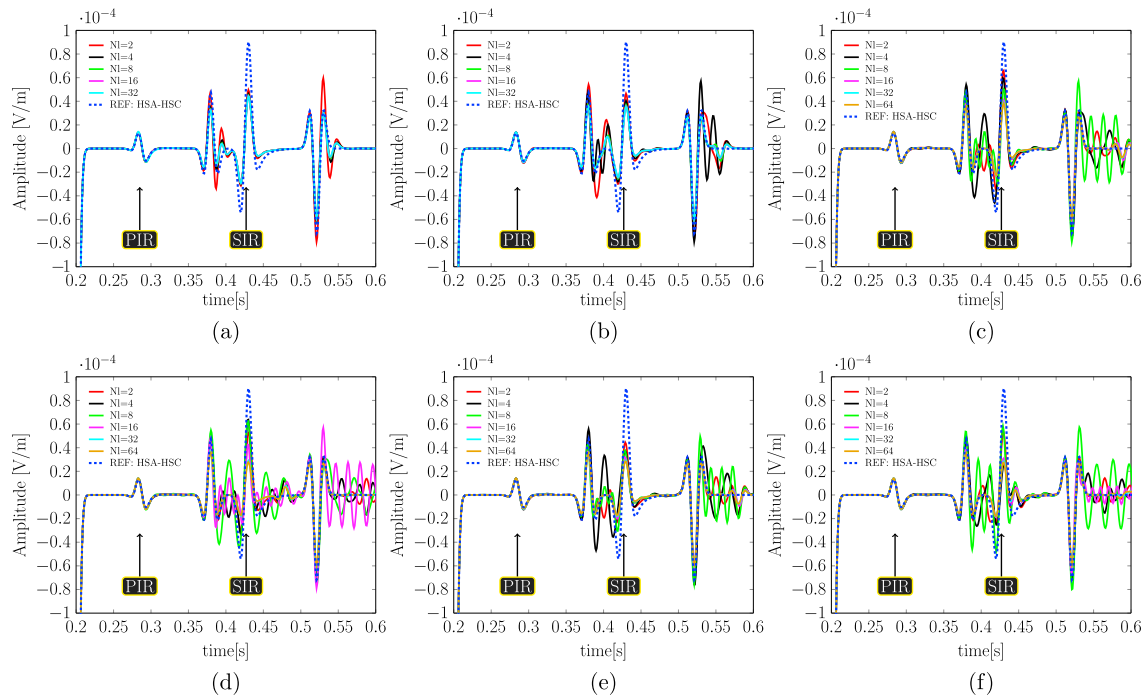


Figure 8. Response for thin-bed geometries of the form A-C-B-C, varying with the amount of layers NI for package thicknesses (a) 20 m, (b) 40 m, (c) 80 m, (d) 160 m, (e) 70 m (dominant S wavelength), and (f) 105 m (dominant P wavelength).

in the signal strengthening or weakening of the IR fields. One can observe that the reference response of hs A- hs C indeed has a higher S wave-related IR field than the reference response of hs A-hs B due to the higher contrast in coupling coefficients. However, remarkable is the fact that additional thin-bed contrasts decrease the SIR in case of packages of thin beds that have alternating thin beds starting with medium C over medium B (a negative coupling coefficient contrast) but increase the SIR when the thin-bed alternations start with medium B over medium C (a positive coupling coefficient contrast).

Intuitively, the controlling factor seems to be whether the package of thin beds starts with a positive or negative contrast in coupling coefficient. To focus on the effect of contrasts in coupling coefficients, we will now briefly investigate what happens to the thin-bed responses when we change the electrolyte concentrations in the pore fluid.

4.3. Different Electrolyte Concentrations in the Pore Fluid

The electrolyte concentration in the pore fluid directly influences the zeta potential. For example, the empirical study by *Pride and Morgan [1991]* found

$$\zeta^P = 8 + 26\log_{10}C, \tag{8}$$

to be a reasonable approximation of the zeta potential (with the zeta potential in millivolts). Here C denotes the electrolyte concentration of the pore fluid in mol/L. *Revil et al. [1999]* have demonstrated this equation from first principles using electrical double-layer theory. They provide a physical explanation for the two constants that appear in equation (8). As we have seen, the zeta potential on its turn directly influences the value of the static seismo-electromagnetic coupling coefficient \mathcal{L}_0 (equation (6)).

Several laboratory studies have shown that a higher ionic concentration leads to a lower seismo-electromagnetic coupling coefficient and a weaker observed seismo-electromagnetic effect [e.g., *Schoemaker, 2011; Zhu and Toksöz, 2013*]. We here focus solely on the effect of changing electrolyte concentrations. Therefore, all other seismo-electromagnetic input model parameters are chosen equal to each other for all three media (media A, B, and C), resulting in (more or less) equal seismic velocities for all media. Since there are no seismic velocity contrasts, there are no coseismic reflection arrivals to be expected in the records. The parameters that directly or indirectly depend on the electrolyte concentration of course do change accordingly (e.g., fluid conductivity), resulting in differences in the electromagnetic velocities between the three media.

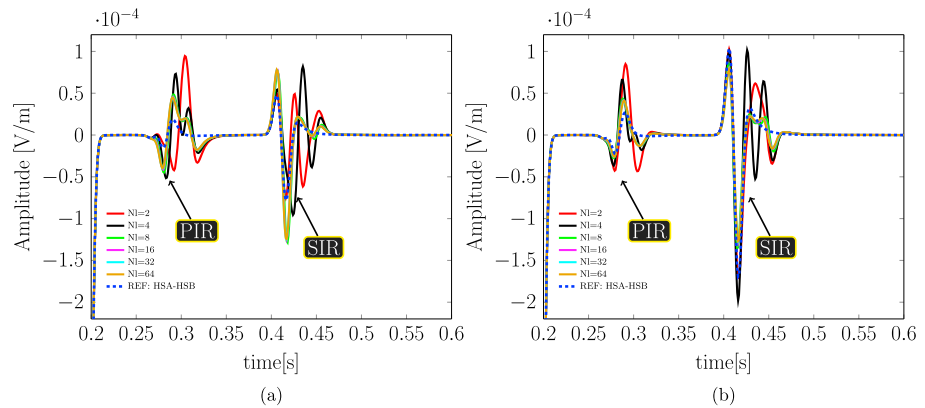


Figure 9. Response for thin-bed geometries of the form A-B-C-B, varying with the amount of layers NI for package thickness PT = 80 and varying coupling coefficients. (a) Relative distribution of coupling coefficients: medium A < medium B < medium C. (b) Relative distribution of coupling coefficients: medium A < medium C < medium B.

We use a package of PT = 80 m, with structure A-B-C-B. The electrolyte concentrations are chosen such that medium A has the highest electrolyte concentration of $1 \cdot 10^{-4}$ mol/L and hence the lowest coupling coefficient with a value of $9.07 \cdot 10^{-9} \text{ m}^2 \text{ s V}^{-1}$. We vary the relative distribution of concentrations between media B and C, using values of $1 \cdot 10^{-5}$ mol/L and $1 \cdot 10^{-6}$ mol/L. In this way, either medium B has a higher concentration than medium C or vice versa. The corresponding coupling coefficients are $1.15 \cdot 10^{-8} \text{ m}^2 \text{ s V}^{-1}$ and $1.4 \cdot 10^{-8} \text{ m}^2 \text{ s V}^{-1}$, respectively. The contrast in coupling coefficient between medium A and the package of thin-bed PT now has a negative contrast (opposite to the results of Figure 6a). The results are presented in Figure 9. Figure 9a shows the results where medium C has a higher coupling coefficient than medium B, resulting in a negative thin-bed contrast within the package PT (since PT starts with medium B over medium C). We observe, focusing on the first peak of the SIR, that with increasing NI, the SIR response slightly increases as well. Figure 9b presents the results where medium B has a higher coupling coefficient than medium C, resulting in a positive thin-bed contrast within the package PT. We now observe that with increasing NI, the SIR decreases. At first sight, this seems to be contradicting with the observations of Figure 6a, where a positive thin-bed contrast within package PT resulted in increasing SIR with increasing NI, and a negative contrast resulted in decreasing SIR with increasing NI. However, there is another difference between the experiments resulting in Figures 6a and 9. In Figure 6a, the contrast between medium A and the package of thin-bed PT was positive, whereas for Figure 9, this contrast is negative. In both cases, when the combined result of the contrast between upper half-space and package of thin beds, and the internal thin-bed contrast is positive, constructive interference occurs, whereas destructive interference occurs when the combined contrast is negative. We can also observe in Figure 9b that a higher contrast between media A and B results in a higher reference response SIR. Besides the above observations, we can observe that the PIR response in these experiments is also affected by the presence of thin beds. In Figure 9a we can see that the PIR has a smaller reference response than in Figure 9b, but has a signal strengthening due to the presence of thin beds. We can also observe that the PIR waveform is slightly changed (this also slightly occurs for the SIR). This impedes the interpretation of the interference patterns: it is difficult to determine whether signal strengthening or weakening occurs with increasing NI.

4.4. Random Models

To exclude the possibility of introduced artifacts due to the periodicity of the thin-bed models under consideration, we investigate the signal interference patterns for a model with package thickness PT = 80 m, where the added sublayers have either arbitrary arbitrarily chosen by the user or mathematically random bed thicknesses. The random bed thicknesses are determined using a single uniformly distributed random number generator in the interval (0,1), which calculates the random positions (for a fixed amount) of the interfaces as a fraction of the sum of the random numbers times the fixed package thickness. In other words, each layer is a random fraction of the package thickness. We increase “randomization” going from arbitrary models to random models. We still vary the amount of sublayers NI as we did before, with the pattern A-B-C-B and so on. The results are presented in Figure 10a for arbitrary bed thicknesses and in Figure 10b for random bed thicknesses.

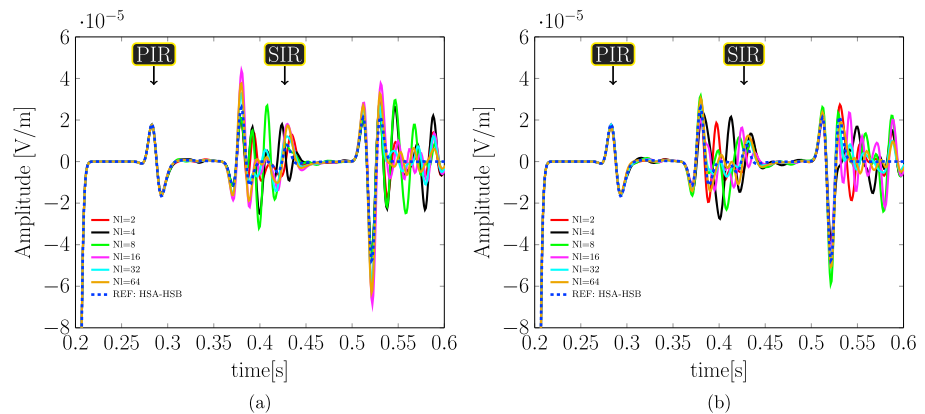


Figure 10. Response for thin-bed geometries of the form A-B-C-B, varying with the amount of layers NI for a package thickness of 80 m and with (a) arbitrary bed thicknesses and (b) random bed thicknesses.

We compare the results of Figure 10 with the result of the periodic thin-bed experiments for a package thickness $PT = 80$ m with equally thick thin beds as presented earlier in Figure 6a. We can clearly observe similar signal-enhancing interference patterns for the shear wave-related IR field. We can again observe that for increasing amounts of sublayers, the multiple arrivals from the relatively thick sublayers (low amount of sublayers) are being compressed and map at the arrival time of the shear wave-related IR field. However, where in the periodic case the line representing a total of 64 sublayers ($NI = 64$) yields the largest signal strength for the shear wave-related IR field, in the case of arbitrary sublayer thickness of Figure 10a, both $NI = 16$ and $NI = 64$ result in the largest signal strength. Looking more closely, we can still observe that for $NI = 64$, small multiples are being observed, for example, at times slightly less than $t = 0.43$ s. This might indicate that for $NI = 64$ and $PT = 80$ m, the seismo-electromagnetic signal still did not fully reach its maximum thin-bed sensitivity in thin-bed settings with arbitrary bed thickness. When we increase the randomness of the bed thickness, we can again observe that the multiples are being compressed with increasing NI, and also the maximum amplification for $NI = 64$ is less than in the case of periodic and arbitrary layering. Furthermore, there seems to be a slightly bigger phase shift on the SIR responses for different NI in case of completely random bed thicknesses. Overall, the interference patterns between Figures 6a, 10a, and 10b look very similar, with similar multiple convergence pattern. Therefore, we can conclude that the earlier discussed interference patterns are not artifacts due to the periodicity of the sublayer thickness, but represent seismo-electromagnetic signal-enhancing (or destructing) interference mechanisms. Nevertheless, there seems to be a higher amplification of the SIR when the thin-bed thicknesses are less random. Also, the multiples seem to converge at smaller NI in scenarios with less randomness for the bed thicknesses (or in other words, higher periodicity).

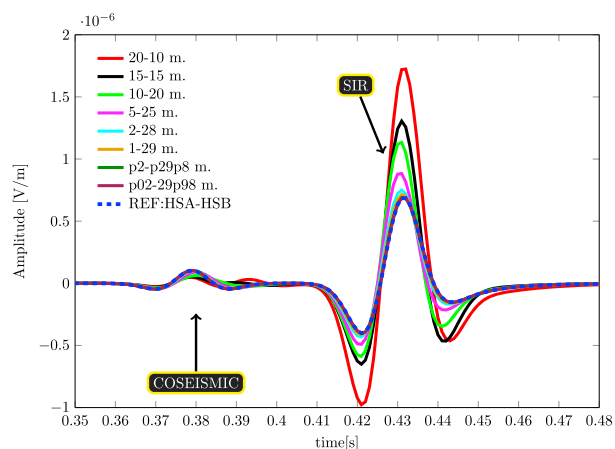


Figure 11. Oil-water monitoring.

Table 2. Overview of the Relevant Parameters and Wave/Field Velocities for Each of the Different Media (Only the Deviations From Table 1 Are Presented)^a

Physical Quantity	Medium A (Top hs)	Medium B (Layer or hs)	Effective Parameters Oil Layer
Electric conductivity fluid σ^f (S/m)	0.93	0.93	0.19
Complex electric conductivity $\hat{\sigma}^e$ (S/m)	0.12	$6.18 \cdot 10^{-2}$	$1.24 \cdot 10^{-2}$
Electrolyte concentration pore fluid C (mol L ⁻¹)	$1.0 \cdot 10^{-2}$	$1.0 \cdot 10^{-2}$	0.002
Relative electric permittivity fluid ϵ_r^f (-)	70	70	20.4
Viscosity pore fluid η (N s m ⁻²)	$1 \cdot 10^{-3}$	$1 \cdot 10^{-3}$	$1.4 \cdot 10^{-3}$
Bulk modulus fluid K^f (N m ⁻²)	$2.25 \cdot 10^9$	$2.25 \cdot 10^9$	$1.49 \cdot 10^9$
Fluid density ρ^f (kg m ⁻³)	$1.0 \cdot 10^3$	$1.0 \cdot 10^3$	$9.32 \cdot 10^2$
Static coupling coefficient \mathcal{L}_0 (m ² s V ⁻¹)	$3.64 \cdot 10^{-9}$	$1.82 \cdot 10^{-9}$	$5.35 \cdot 10^{-10}$
Zeta potential double layer ζ^p (V)	$-4.4 \cdot 10^{-2}$	$-4.4 \cdot 10^{-2}$	$-6.22 \cdot 10^{-2}$
P wave velocity (m/s)	3166.73–3166.76	3163.19–3163.19	3015.65–3015.66
Slow P wave velocity (m/s)	2.91–93.74	4.00–131.93	2.98–96.96
S wave velocity (m/s)	2110.79–2110.87	1952.83–1953.03	1958.49–1958.57
EM velocity (m/s)	$3179.63-1.01 \cdot 10^5$	4496.68–142233.38	10054.89–318044.72

^aMedia A and B are water saturated. To illustrate the frequency dependency of certain wave/field types, velocity ranges (the real parts of the complex velocities) are displayed for the bandwidth under consideration. Note that the EM velocities are proportional to the square root of frequency.

4.5. Reservoir Monitoring: Oil-Water Contacts

We now focus on the sensitivity of the seismo-electromagnetic signals to different saturating fluids. We investigate what happens when the relative thickness of two different saturating fluids in a fixed package of rock of 30 m thickness (representing a reservoir) changes. To this end, we simulate a medium, where the thickness of an oil layer decreases and the thickness of a water layer increases. This situation occurs, for example, in an oil reservoir during production. The starting-thickness ratio is 20 m oil layer and 10 m water layer. The water layer is fully saturated, the oil layer has 80% oil saturation and 20% water saturation. This leads to the relevant medium parameters as presented in Table 2 (only the values differing from Table 1 are presented), where the effective values for the oil layer are displayed (i.e., saturation has already been taken into account). We have included the effect of saturation in a linear manner, which is allowed due to the volume-averaging principles that *Pride* [1994] applied in deriving the seismo-electromagnetic theory. For viscosity, we have used a logarithmic version of linear addition, as presented by *Warden et al.* [2013]. Figure 11 displays the results of the oil-water production simulation. The reference response is the seismo-electromagnetic response from hs A over hs B, where both half-spaces are fully water saturated. Looking at the purely seismic information of the coseismic fields, we can observe a phase delay due to dispersion related to the presence of (the more viscous) oil. In addition, we can observe that the presence of oil has a signal-enhancing effect on the SIR field. The highest signal strength occurs for the thickest oil layer: 20 m oil layer, 10 m water layer, in other words the starting thickness ratio of this model. During oil production, when the water content in the 30 m package increases and the oil layer gets thinner, the shear wave-related IR signal strength weakens. Furthermore, we can observe that the seismo-electromagnetic signal is very sensitive to the oil-water contact: an oil layer of 0.2 m thickness (the line representing p2-29p8) is still slightly recognized. Once the oil layer thickness reaches 0.02 m, the corresponding line overlaps with the reference response, indicating that the seismo-electromagnetic signal does not sense the presence of oil anymore. The thickness of 0.2 m is far below the dominant wavelength of the seismic shear wave generating this SIR, which is about 70 m. According to *Widess* [1973], beds with thicknesses less than 1/8 of this dominant wavelength, 8.75 m, are considered thin beds. The seismo-electromagnetic signal clearly has a very high sensitivity to the presence of oil-water contacts.

5. Discussion

We have studied the effect of changing electrolyte concentrations in the pore fluid on the seismo-electromagnetic interference patterns. Unfortunately, we cannot directly link these effects to the changing seismo-electromagnetic coupling coefficient only: for example, the fluid conductivity also changes with changing electrolyte concentration, thereby affecting the electromagnetic velocities. However, it seems reasonable to address the observed changes to changes in the seismo-electromagnetic coupling coefficients, since physically speaking these coefficients control the amount of coupling between mechanical waves and

electromagnetic fields. For other seismo-electromagnetic parameters, it is even harder to uniquely determine the effect of that specific parameter on the thin-bed interference patterns, since most seismo-electromagnetic parameters are mutually related. We have of course considered a simple situation where we only changed the electrolyte concentration of the pore fluid. In reality, the chance that between different media other medium properties also vary is high. Nevertheless, for monitoring purposes of, for example, oil or gas production, this is an interesting observation, since we purely focus on changes in the saturating pore fluid and assume that the rest of the reservoir remains the same. Despite probable changes in permeability during production, this is a reasonable first assumption.

Our simplified oil/water contact modeling experiments simulating oil production have proven that seismo-electromagnetic signals are very sensitive to oil-water contacts. This observation has previously been made in laboratory experiments [e.g., *Smeulders et al.*, 2014]. We have modeled a situation with two immiscible fluids using an approximative theory [*Pride*, 1994] in which the capillary effects are neglected. This approach is unable to describe all physical mechanisms involved in the wave propagation and attenuation in porous media containing two immiscible fluids. As an alternative, the formulations of *Revil and Mahardika* [2013] could be used. However, macroscopically, we believe that the observed sensitivity effects of seismo-electromagnetic signals to oil/water contrasts are still valid, and only in terms of amplitudes or exact interference patterns differences might occur when using the formulation of *Revil and Mahardika* [2013]. In our oil/water experiment, we have observed that during oil production, when the water content in the 30 m package increases and the oil layer gets thinner, the SIR signal strength weakens. However, as we have also seen, effective strengthening or weakening of thin-bed responses seems to be determined by the contrasts in seismo-electromagnetic coupling coefficient. In the laboratory experiments by *Smeulders et al.* [2014], an increasing interface response with decreasing oil bed thickness was observed. However, this can probably be explained due to the fact that in this laboratory experiment, a porous sample was placed in a water tank. The pressure wave generated by the source in the water, therefore, experiences a contrast between pure water on both sides of the sample (where the seismo-electromagnetic coupling coefficient is zero) and a porous medium. The contrasts in coupling coefficients are then clearly different from our modeled contrast, and therefore, it is logical that different effects on the interface response signal are observed, as we have also seen in our varying electrolyte modeling experiments. However, now that we schematically have simulated an oil reservoir during production, we can use ESSEMOD to try and validate, as a next step, the oil/water contact seismo-electromagnetic laboratory experiments as presented by *Smeulders et al.* [2014].

Since we of course only modeled a few scenarios and contrasts, we do not exclude that different interference patterns might occur in, for example, media with different medium parameters for the thin beds and thin-bed contrasts or, for example, when investigating different seismo-electromagnetic source-receiver combinations. Also, in our varying electrolyte simulations, the upper half-space always had the lowest coupling coefficient. Different interference patterns are to be expected when the upper half-space has a coupling coefficient that has a value that lies, for example, in between the coupling coefficients of the thin-bed layers. Besides focusing at amplitude changes, one could also try to study and exploit the fact that interference patterns can cause phase shifts and waveform changes as well.

Are thin-bed geological structures the solution for the weak signal-to-noise ratio of the seismo-electromagnetic signals that limits the use of this technique in the geophysical community? Probably not. What is more important is the awareness that thin-bed geological settings can have serious consequences for the recorded seismo-electromagnetic interface response signals, due to complex interference patterns. For example, a strong response in the record might be due to a strong reflector/contrast, but might also be the effect of signal strengthening/weakening due to the presence of thin beds. Due to the complexity of the interference patterns and the many possible parameter combinations that can influence these patterns, it is very difficult to find effective medium expressions that properly describe the response of the package of thin beds.

In reality, we of course cannot control the thickness of the beds that we encounter in the field and also not the order of the contrasts (determining constructive or destructive interference). However, we have seen that we can distinguish two limits of bed thickness: an upper limit of bed thickness that determines whether the individual layers are still recognized or not and a lower limit that determines the border from whereon further thinning does not affect the seismo-electromagnetic IR signal strength anymore. To have an effective medium response, the beds need to be thinner than the upper limit. The lower limit determines the maximum signal strengthening or weakening that can occur, together with the total package thickness of the thin beds.

The maximum amplitude tuning occurs for package thicknesses similar to the dominant wavelengths of the P and S waves. We can take this knowledge into account in our acquisition design. By changing the dominant frequencies of the seismic source signal, we can effectively change the optimal tuning package thickness for the generated waves. When we have a geological setting where constructive interference occurs, we can try to optimize the amplitude tuning effects by playing with the source bandwidth. Combined with, for example, velocity analysis, this determined dominant wavelength can assist in determining the thin-bed package thickness of the subsurface. Can we obtain the desired factor of amplitude enhancement that we need to measure the seismo-electromagnetic signals? We are not sure. However, the investigation presented in this paper is carried out only for one seismo-electromagnetic source-receiver combination and certain geological models. Different models can result in different interference patterns that might lead to even greater amplifying effects. Furthermore, there might be differences in signal enhancing for different seismo-electromagnetic source-receiver combinations. Depending on, for example, the geological properties as obtained from boreholes, the optimal seismo-electromagnetic source-receiver combination can be determined (i.e., the combination that is to be expected to experience maximum signal strengthening) for the specific geological setting under consideration and hence be taken into account in the seismo-electromagnetic acquisition design, e.g., which source and receiver types to deploy. In addition, not only amplitude changes but also phase and waveform changes have been observed. These phase and waveform changes could be useful as well but require additional investigation.

In this paper, we have not focused on the sensitivity of coseismic fields to thin-bed structures. It is important to realize that coseismic electromagnetic fields can only provide localized information (at the receivers), since they copropagate within the seismic waves. Therefore, all seismo-electromagnetic information of the subsurface thin-bed structures has been lost from the signal once the coseismic fields reach the receivers at the surface. The only information of the thin-bed structures left in the signal is purely seismic information (and we have seen that seismic signals are less sensitive to thin beds than seismo-electromagnetic fields). Nevertheless, there might still be some useful seismic information in the coseismic fields, for example, the observed phase delay due to dispersion related to the presence of (the more viscous) oil.

The challenge of the weak seismo-electromagnetic signal-to-noise ratio is unfortunately not solved yet. It is important to be aware that nature can help us in the form of thin-bed geology but can also make our lives more difficult due to complex signal interference patterns that are hard to describe in terms of an effective medium. We could try to take these geological settings into account in our acquisition designs and the way we use our seismo-electromagnetic sources. Existing seismo-electromagnetic signal-enhancing techniques like seismo-electromagnetic focusing or specific filtering techniques combined with a search for optimal natural signal enhancements due to thin-bed geology could be a way forward. Combined efforts might yield the desired amplification factor that is required for industrial and global geophysical applications.

6. Conclusions

Using numerical seismo-electromagnetic wave propagation experiments through packages of thin beds, we have shown that thin-bed geological settings can improve the signal strength of the seismo-electromagnetic interface response fields. Increasing amounts of thin beds can cause the shear wave-related interface response strength to increase or decrease. In our experiments, the pressure wave-related interface response fields are not visibly affected by the presence of thin beds.

Both the thickness of the thin beds as well as the amount of thin beds play a role in whether or not the multiples (created by the individual thin beds) vanish in the record (i.e., are compressed at the position of the shear wave-related interface response field in the reference response (the response for which there are no thin beds present)). We can distinguish two limits of bed thickness: an upper limit and a lower limit. The upper limit of bed thickness determines whether the individual layers are still recognized or not. When beds are thinner than this limit, the package of thin beds starts acting like an effective medium and the multiples vanish from the record. The lower limit of bed thickness determines the border from whereon further thinning does not affect the seismo-electromagnetic IR signal strength anymore, because the bed thickness is below the sensitive resolution of the seismo-electromagnetic fields. The upper limit seems to occur when the thin-bed thickness reaches a value of around 5 m thickness. This corresponds to thicknesses of 1/14 and 1/21 of the dominant S and P wavelengths in our models, 70 m and 105 m, respectively. The lower limit, from whereon

further thinning does not affect the signal strength anymore, seems to occur around the 2.5 m thickness. This lower limit corresponds to 1/28 and 1/42 of the dominant S and P wavelengths, respectively. This is far below the conventional seismic definition of a thin bed.

Tuning package thickness experiments of 70 m and 105 m show that there seems to be a maximum strengthening of the shear wave-related interface response signal of a factor 3 for these package thicknesses. This is an indication that not only the amount of thin beds and the thin-bed thickness but also the package thickness itself plays an important role in the amplification of the shear wave-related interface response fields due to thin-bed geological structures. The maximum amplitude tuning occurs for package thicknesses similar to the dominant wavelengths of the P and S waves.

Whether the thin beds result in an effective strengthening or weakening of the signal seems to be determined by the contrast in seismo-electromagnetic coupling coefficients between the different thin beds. Specific experiments where the electrolyte concentration of the pore fluid was varied have shown that when the combined result of the coupling coefficient contrast between the upper half-space and package of thin beds and the internal thin-bed contrast itself is positive, constructive interference occurs, whereas destructive interference occurs when the combined contrast is negative. Other interference patterns can occur for other combinations of contrasts, impeding the description of seismo-electromagnetic thin-bed responses in terms of effective media.

Arbitrary (user chosen) and mathematically random bed thickness modeling experiments resulted in responses that are very similar to the periodic bed thickness results. We can therefore conclude that the observed seismo-electromagnetic interference patterns are not artifacts due to the periodicity of the bed thickness but truly seismo-electromagnetic signal-enhancing (or destructing) interference mechanisms. Nevertheless, there seems to be a higher amplification of the shear wave-related interface response fields when the thin-bed thicknesses are less random. Also, the multiples generated by the individual thin beds seem to converge at smaller amounts of thin beds in scenarios with less randomness for the bed thicknesses (higher bed periodicity).

Our oil/water contact modeling experiments where the oil layer is gradually thinned prove that the seismo-electromagnetic signal has a very high sensitivity to oil-water contacts: an oil layer with 20% water saturation and of 0.2 m thickness, a thickness of about $\frac{1}{350}$ of the dominant wavelength of the shear wave generating this response is still slightly recognized. This is a clear indicator of the high seismo-electromagnetic sensitivity for different saturating fluids.

Acknowledgments

This research was funded as a Shell Global Solutions International B.V.-FOM (Fundamental Research on Matter) project within the research program "Innovative physics for oil and gas." The authors are grateful to Jan Thorbecke for his help coding ESSEMOD, Ranajit Ghose for useful suggestions, Rick Donselaar and Jan-Kees Blom for geological discussions, Max Holicki for graphical TikZ support, and several researchers from the Earth Resources Laboratory (Massachusetts Institute of Technology, USA) for constructive and inspiring discussions. The data used in this paper are generated by the numerical modeling code ESSEMOD and can be requested from the authors.

References

- Biot, M. A. (1956), Theory of propagation of elastic waves in a fluid-saturated porous solid. I. Low-frequency range, *J. Acoust. Soc. Am.*, *28*, 168–178.
- Butler, K. E., R. Don Russell, A. W. Keping, and M. Maxwell (1996), Measurement of the seismoelectric response from a shallow boundary, *Geophysics*, *61*, 1769–1778.
- Cagniard, L. (1953), Basic theory of the magneto-telluric method of geophysical prospecting, *Geophysics*, *18*, 605–635.
- Carbajal, M., N. Linde, and T. Kalscheuer (2012), Focused time-lapse inversion of radio and audio magnetotelluric data, *J. Appl. Geophys.*, *84*, 29–38.
- Carcione, J., C. Morency, and J. Santos (2010), Computational poroelasticity—A review, *Geophysics*, *75*(5), 75A229–75A243.
- Colombo, D., and M. De Stefano (2007), Geophysical modeling via simultaneous joint inversion of seismic, gravity, and electromagnetic data: Application to prestack depth imaging, *Leading Edge*, *26*, 326–331.
- Colombo, D., G. McNeice, E. Curiel, and A. Fox (2013), Full tensor CSEM and MT for subsalt structural imaging in the Red Sea: Implications for seismic and electromagnetic integration, *Leading Edge*, *32*, 436–449.
- Constable, S. (2010), Ten years of marine CSEM for hydrocarbon exploration, *Geophysics*, *75*(5), 75A67–75A81.
- Dean, T., and J. C. Dupuis (2011), The vibroelectric method—A new tool for near-surface characterisation and improved seismic data quality, paper presented 73rd European Association of Geoscientists and Engineers Conference and Exhibition Incorporating SPE EUROPEC, EAGE, Vienna, Austria, 23–25 May.
- Dean, T., C. Dupuis, R. Herrmann, and J. Valuri (2012), A brute-strength approach to improving the quality of seismoelectric data, paper presented at Annual Meeting of the Society of Exploration Geophysicists (SEG), SEG, Las Vegas, Nev., 4–9 Nov.
- Dietrich, M., and S. Garambois (2013), Some theoretical and practical questions in transient electrokinetic coupling in fluid-saturated porous media, in *Poromechanics V: Proceedings of the Fifth Biot Conference on Poromechanics*, pp. 299–305, Biot Conference on Poromechanics, Vienna, Austria.
- Feld, R., and E. Slob (2014), *GPR Without a Source by Use of Interferometry by Multi-Dimensional Deconvolution*, Soc. Explor. Geophys., pp. 844–849, Denver, Colo.
- Frenkel, J. (1944), On the theory of seismic and seismoelectric phenomena in moist soil, *J. Phys.*, *8*, 230–241.
- Fujinawa, Y., and Y. Noda (2015), Characteristics of seismoelectric wave fields associated with natural microcracks, *Pure Appl. Geophys.*, *173*, 255–268.

- Fujinawa, Y., K. Takahashi, Y. Noda, H. Itaka, and S. Yazaki (2011), Remote detection of the electric field change induced at the seismic wave front from the start of fault rupturing, *Int. J. Geophys.*, 2011, 752193.
- Garambois, S., and M. Dietrich (2001), Seismoelectric wave conversions in porous media: Field measurements and transfer function analysis, *Geophysics*, 66-5, 1417–1430.
- Garambois, S., and M. Dietrich (2002), Full waveform numerical simulations of seismo-electromagnetic wave conversions in fluid-saturated stratified porous media, *J. Geophys. Res.*, 107, 2148, doi:10.1029/2001JB000316.
- Grobbe, N., and E. Slob (2013), Validation of an electroseismic and seismoelectric modeling code, for layered Earth models, by the explicit homogeneous space solutions, in *SEG Technical Program Expanded Abstracts*, pp. 1847–1851, Soc. of Explor. Geophys., doi:10.1190/segam2013-1208.1.
- Grobbe, N., J. Hunziker, and E. Slob (2014), Seismoelectric wave propagation modeling for typical laboratory configurations: A numerical validation, *SEG Technical Program Expanded Abstracts 2014*, pp. 2072–2077, Soc. of Explor. Geophys., doi:10.1190/segam2014-0689.1.
- Guha, S., S. Kruse, E. Wright, and U. Kruse (2005), Spectral analysis of ground penetrating radar response to thin sedimentary layers, *Geophys. Res. Lett.*, 32, L23304, doi:10.1029/2005GL023933.
- Haartsen, M., and S. Pride (1997), Electrostatic waves from point sources in layered media, *J. Geophys. Res.*, 102-B11, 24,745–24,769.
- Haines, S. S., and S. R. Pride (2006), Seismoelectric numerical modeling on a grid, *Geophysics*, 71-6, N57–N65.
- Hunziker, J., E. Slob, and K. Wapenaar (2011), Time-lapse controlled-source electromagnetics using interferometry, *Leading Edge*, 30, 564–567.
- Hunziker, J., J. Thorbecke, and E. Slob (2014), Probing the solution space of an EM inversion problem with a genetic algorithm, *SEG Technical Program Expanded Abstracts 2014*, pp. 833–837, Soc. of Explor. Geophys., doi:10.1190/segam2014-0293.1.
- Ivanov, A. (1940), Seismoelectric effect of the second kind (in Russian), *Bull. Acad. Sci. USSR, Série Géogr. Géophys.*, 5, 699–727.
- Jardani, A., and A. Revil (2015), Seismoelectric couplings in a poroelastic material containing two immiscible fluid phases, *Geophys. J. Int.*, 202, 850–870.
- Jardani, A., A. Revil, E. Slob, and W. Söllner (2010), Stochastic joint inversion of 2D seismic and seismoelectric signals in linear poroelastic materials, *Geophysics*, 75(1), N19–N31.
- Johnson, D. (1989), Scaling function for dynamic permeability in porous media, *Phys. Rev. Lett.*, 63(5), 580–580.
- Johnson, D., J. Koplik, and R. Dashen (1987), Theory of dynamic permeability and tortuosity in fluid-saturated porous media, *J. Fluid Mech.*, 176, 379–402.
- Jouniaux, L., and J. Pozzi (1995), Permeability dependence of streaming potential in rocks for various fluid conductivities, *Geophys. Res. Lett.*, 22, 485–488.
- Jouniaux, L., M. Bernard, M. Zamora, and J. Pozzi (2000), Streaming potential in volcanic rocks from Mount Pelée, *J. Geophys. Res.*, 105(B4), 8391–8401.
- Kröger, B., U. Yaramanci, and A. Kemna (2014), Numerical analysis of seismoelectric wave propagation in spatially confined geological units, *Geophys. Prospect.*, 2014, 133–147.
- Kruse, S., M. Grasmueck, M. Weiss, and D. Viggiano (2006), Sinkhole structure imaging in covered karst terrain, *Geophys. Res. Lett.*, 33, L16405, doi:10.1029/2006GL026975.
- Marshall, D., and T. Madden (1959), Induced polarization, a study of its causes, *Geophysics*, 24, 790–816.
- Morgan, F., E. Williams, and T. Madden (1989), Streaming potential properties of westerly granite with applications, *J. Geophys. Res.*, 94(B9), 12,449–12,461.
- Oldenburg, D., and Y. Li (1994), Inversion of induced polarization data, *Geophysics*, 59, 1327–1341.
- Pride, S. (1994), Governing equations for the coupled electromagnetics and acoustics of porous media, *Phys. Rev. B*, 50-21, 15,678–15,696.
- Pride, S., and F. Morgan (1991), Electrokinetic dissipation induced by seismic waves, *Geophysics*, 56, 914–925.
- Pride, S. R., and S. Garambois (2005), Electrostatic wave theory of Frenkel and more recent developments, *J. Eng. Mech.*, 131, 898–907.
- Pride, S. R., and M. W. Haartsen (1996), Electrostatic wave properties, *J. Acoust. Soc. Am.*, 100, 1301–1315.
- Ren, H., X. Chen, and Q. Huang (2012), Numerical simulation of coseismic electromagnetic fields associated with seismic waves due to finite faulting in porous media, *Geophys. J. Int.*, 188, 925–944.
- Revil, A., and N. Florsch (2010), Determination of permeability from spectral induced polarization in granular media, *Geophys. J. Int.*, 181, 1480–1498.
- Revil, A., and H. Mahardika (2013), Coupled hydromechanical and electromagnetic disturbances in unsaturated porous materials, *Water Resour. Res.*, 49, 744–766.
- Revil, A., P. Pezard, and P. Glover (1999), Streaming potential in porous media 1. Theory of the zeta potential, *J. Geophys. Res.*, 104(B9), 20,021–20,031.
- Revil, A., V. Naudet, J. Nouzaret, and M. Pessel (2003), Principles of electrography applied to self-potential electrokinetic sources and hydrogeological applications, *Water Resour. Res.*, 39, 1114, doi:10.1029/2001WR000916.
- Revil, A., N. Linde, A. Cerepi, D. Jougnot, S. Matthäi, and S. Finsterle (2007), Electrokinetic coupling in unsaturated porous media, *J. Colloid Inter. Sci.*, 313, 315–327.
- Revil, A., G. Barnier, M. Karaoulis, P. Sava, A. Jardani, and B. Kulesa (2013), Seismoelectric coupling in unsaturated porous media: Theory, petrophysics, and saturation front localization using an electroacoustic approach, *Geophys. J. Int.*, 196, 867–884.
- Revil, A., A. Jardani, P. Sava, and A. Haas (2015), *The Seismoelectric Method: Theory and Application*, John Wiley, Hoboken, N. J.
- Robertson, J. D., and H. H. Nogami (1984), Complex seismic trace analysis of thin beds, *Geophysics*, 49, 344–352.
- Rubino, J., G. Castromán, T. Müller, L. Monachesi, F. Zyserman, and K. Holliger (2015), Including poroelastic effects in the linear slip theory, *Geophysics*, 80(2), A51–A56.
- Sambuelli, L., L. Socco, and L. Brecciaroli (1999), Acquisition and processing of electric, magnetic and GPR data on a Roman site (Victimulae, Salussola, Biella), *J. Appl. Geophys.*, 41, 189–204.
- Sava, P., and A. Revil (2012), Virtual electrode current injection using seismic focusing and seismoelectric conversion, *Geophys. J. Int.*, 191, 1205–1209.
- Sava, P., A. Revil, and M. Karaoulis (2014), High definition cross-well electrical resistivity imaging using seismoelectric focusing and image-guided inversion, *Geophys. J. Int.*, 198, 880–894.
- Schakel, M., and D. Smeulders (2010), Seismoelectric reflection and transmission at a fluid/porous medium interface, *J. Acoust. Soc. Am.*, 127, 13–21.
- Schakel, M. D., D. M. J. Smeulders, E. C. Slob, and H. K. J. Heller (2011), Laboratory measurements and theoretical modeling of seismoelectric interface response and coseismic wave fields, *J. Appl. Phys.*, 109, 74903.
- Schoemaker, F. C. (2011), Electrokinetic conversion, PhD thesis, Delft Univ. of Technol., Aula TU Delft.

- Schoemaker, F. C., N. Grobbe, M. D. Schakel, S. A. L. de Ridder, E. C. Slob, and D. M. J. Smeulders (2012), Experimental validation of the electrokinetic theory and development of seismoelectric interferometry by cross-correlation, *Int. J. Geophys.*, *514242*, 23.
- Smeulders, D. M. J., N. Grobbe, H. K. J. Heller, and M. D. Schakel (2014), Seismoelectric conversion for the detection of porous medium interfaces containing water and oil, *Vadose Zone J.*, *13*(5), 1–7, doi:10.2136/vzj2013.06.0106.
- Thompson, A. H., et al. (2007), Field tests of electroseismic hydrocarbon detection, *Geophysics*, *72*(1), N1–N9.
- Thompson, R. (1936), The seismic electric effect, *Geophysics*, *1*, 327–335.
- Valuri, J., T. Dean, and J. Dupuis (2012), Seismoelectric acquisition in an arid environment, *22nd International Geophysical Conference and Exhibition*, CSIRO Publ., Australia, 26–29 Feb.
- Vozoff, K. (1972), The magnetotelluric method in the exploration of sedimentary basins, *Geophysics*, *37*, 98–141.
- Warden, S., S. Garambois, L. Jouniaux, D. Brito, P. Salliac, and C. Bordes (2013), Seismoelectric wave propagation numerical modelling in partially saturated materials., *Geophys. J. Int.*, *194*, 1498–1513.
- Widess, M. B. (1973), How thin is a thin bed, *Geophysics*, *38*, 1176–1180.
- Zhou, H. (2014), *Practical Seismic Data Analysis*, Cambridge Univ. Press.
- Zhu, Z., and M. N. Toksöz (2005), Seismoelectric and seismomagnetic measurements in fractured borehole models, *Geophysics*, *70*(4), F45–F51.
- Zhu, Z., and M. N. Toksöz (2013), Experimental measurements of the streaming potential and seismoelectric conversion in Berea sandstone, *Geophys. Prospect.*, *61*, 688–700.
- Zhu, Z., M. W. Haartsen, and M. N. Toksöz (2000), Experimental studies of seismoelectric conversions in fluid-saturated porous media, *J. Geophys. Res.*, *105*, 28,055–28,064.
- Zyserman, F. I., P. M. Gauzellino, and J. E. Santos (2010), Finite element modeling of SHTE and PSVTM electroseismics, *J. Appl. Geophys.*, *72*, 79–91.